2D Hydro-Mechanical-Chemical modelling of (de)hydration reactions in deforming heterogeneous rock: The periclase-brucite model reaction

Stefan M. Schmalholz[1], Evangelos Moulas[2], Oliver Plümper[3] and Yuri Y. Podladchikov[1,4]

[1]Institute of Earth Sciences, University of Lausanne, 1015 Lausanne, Switzerland

[2]Institut für Geowissenschaften, University of Mainz, Germany

[3]Department of Earth Sciences, Utrecht University, The Netherlands

[4]Faculty of Mechanics and Mathematics, Moscow State University, Russian Federation

Corresponding author: Stefan Schmalholz (stefan.schmalholz@unil.ch)

Key points:

- 2D Hydro-Mechanical-Chemical model couples rock deformation, porous fluid flow and reactions for brucite-periclase (de)hydration reaction
- Rock heterogeneities affect reaction-front propagation and reaction-induced weakening, and cause differences in fluid and rock pressure
- MATLAB code for numerical 2D Hydro-Mechanical-Chemical model is provided

Abstract

Deformation at tectonic plate boundaries involves coupling between rock deformation, fluid flow and metamorphic reactions, but quantifying this coupling is still elusive. We present a new two-dimensional hydro-mechanical-chemical numerical model and investigate the coupling between heterogeneous rock deformation and metamorphic (de)hydration reactions. Rock deformation consists of linear viscous compressible and power-law viscous shear deformation. Fluid flow follows Darcy's law with a Kozeny-Carman type permeability. We consider a closed isothermal system and the reversible (de)hydration reaction: periclase and water yields brucite. In the models, fluid pressure within a circular or elliptical inclusion is initially below the periclase-brucite reaction pressure, and above in the surrounding. Inclusions exhibit a shear viscosity thousand times smaller than for the surrounding, because we assume that periclase-water and brucite regions have different effective viscosities. In models with circular inclusions, solid deformation has a minor impact on the evolution of fluid pressure, porosity and reaction front. Models with elliptical inclusions and far-field shortening generate higher rock pressure inside the inclusion compared to circular inclusions, and show a faster reaction-front propagation. The propagating reaction-front increases the inclusion surface and causes an effective, reaction-induced weakening of the heterogeneous rock. Weakening evolves strongly nonlinear with progressive strain. Distributions of fluid and rock pressure as well as magnitudes and directions of fluid and solid velocities are significantly different. The models mimic basic features of shear zones and plate boundaries and suggest a strong impact of heterogeneous rock deformation on (de)hydration reactions and associated reaction-induced weakening. The applied MATLAB algorithm is provided.

Plain Language Summary

Geodynamic processes at tectonic plate boundaries are complicated because rock deformation, fluid flow and chemical reactions occur simultaneously. Investigating these

coupled processes by direct observations is usually not possible, and investigating them with laboratory experiments is often not feasible. Alternatively, these coupled processes can be investigated with computer simulations. Here, we present a new two-dimensional hydro-mechanical-chemical computer model to investigate the coupling of these processes. We consider a simple and reversible (de)hydration reaction: periclase (magnesium oxide) and water yields brucite (magnesium hydroxide). The initial fluid pressure within a circular or elliptical inclusion is initially below the periclase-brucite reaction pressure, while in the surrounding it is above. Inclusions in the deforming rock are mechanically weaker than the surrounding. Models with elliptical inclusions generate higher rock pressure inside the inclusion compared to circular inclusions, and show a faster reaction-front propagation. The propagating reaction-front causes an effective, reaction-induced weakening of the heterogeneous rock. Fluid and rock pressure as well as magnitudes and directions of fluid and solid velocities are significantly different. The models mimic basic features of shear zones and suggest a strong impact of heterogeneous rock deformation on (de)hydration reactions and associated weakening. The applied MATLAB algorithm is provided.

1. Introduction

The deformation of lithospheric tectonic plates generates major rifts, strike-slip faults and subduction zones and is, hence, a critical process for the evolution of our dynamic planet. Lithosphere deformation involves a complex interplay between heat transfer, rock deformation, fluid flow and metamorphic reactions. Notably, the interplay between heterogeneous rock deformation and metamorphic (de)hydration reactions, such as related to eclogitization or serpentinization, may have a significant impact on the evolution of shear zones, faulting at slow-spreading ridges or plate boundary processes (e.g. Austrheim, 1987; Escartin et al., 1997; Guillot et al., 2015). Hence, quantifying this interplay is essential for understanding coupled plate tectonic processes. At present, however, such quantification remains elusive.

Many metamorphic reactions are intrinsically coupled to fluid flow since they involve the hydration or dehydration of rocks (e.g. Putnis, 2009; Philpotts and Ague, 2016). Such metamorphic (de)hydration reactions occur when ambient pressure and temperature conditions change due to, for example, rock burial and subsequent exhumation (e.g. Putnis, 2009; Philpotts and Ague, 2016). Furthermore, stress and fluid-pressure variations due to tectonic stresses can affect the region of thermodynamic equilibrium of hydrous/anhydrous phases (e.g. Wheeler, 2018; Moulas et al., 2019; Jamtveit et al., 2019). Fluid flow and associated (de)hydration reactions are essential for many first-order phenomena in plate boundary regions, which include fluid cycling through the lithosphere (e.g. John et al., 2011), the evolution of shear zones (e.g. Austrheim, 1987), slow-slip phenomena at subduction zones (e.g. Gomberg et al., 2010), intermediate-depth earthquakes (e.g. Ferrand et al., 2017), reaction-induced rheological weakening of rocks (e.g. Jolivet et al., 2005) or self-sustained densification of the lower crust (e.g. Malvoisin et al., 2020). These reactions may also be of

industrial relevance, for example, for geological carbon sequestration (e.g. Kelemen and Matter, 2008) or volume changes during geothermal energy extraction.

Metamorphic (de)hydration reactions and rock deformation often occur together. From the view point of solid volume and mass changes, there are two end-member scenarios that couple (de)hydration reactions and rock deformation: (1) The volume of the considered solid-fluid system is constant during (de)hydration or (2) the pressure is constrained during (de)hydration while the volume is unconstrained. The first, constant volume, scenario requires mobility, input and loss of the involved elements via dissolution and precipitation processes (e.g. Putnis, 2009). The considered fluid-rock system is open, but its mass exchange evolves in such a way that the rock volume is constant. For the particular case of an open system with constant volume, there is virtually no coupling between (de)hydration reactions and rock deformation, so that (de)hydration reactions can be investigated using pure hydro-chemical (HC) models assuming that velocities of the solid rock are zero (e.g., Plümper et al., 2017). In the second scenario, the volume is not constrained. Volume change occurs if the system is closed, and the elements are redistributing among the stable phases (e.g. Connolly, 1997; Malvoisin et al., 2015). For the case of a closed system with volume change, deformation of the porous solid coupled with (de)hydration reactions must be investigated using a hydro-mechanical-chemical (HMC) model. Volume changes can be significant and may cause considerable deformation and differential stresses in the rock. These stresses can cause fracturing (e.g. Carmichael, 1987; Kelemen and Hirth, 2012; Plümper et al., 2012; Zheng et al., 2018; Evans et al., 2020), for example, during serpentinization (e.g. Kelemen and Hirth, 2012) or transition from anorthosite to eclogite (e.g. Jamtveit et al., 2000).

Furthermore, metamorphic reactions frequently occur during lithosphere deformation, which exhibits shear deformation significantly larger than the volumetric deformation. Deviatoric stresses drive shear deformation, and the mean stress in a deforming rock is, hence,

not lithostatic (e.g. Schmalholz et al., 2014). Moreover, most deforming rock units are mechanically heterogeneous, due to, for example, their layered structure. These heterogeneities typically cause folding and necking in the deforming lithosphere across all geological scales (e.g. Schmalholz and Mancktelow, 2016). Furthermore, active shear zones are usually mechanically weaker than their wall rocks, so that rock units, including active shear zones, represent mechanically heterogeneous systems. Mechanical heterogeneities in deforming rocks cause stress and pressure variations within and around the heterogeneities (e.g. Schmid and Podladchikov, 2003; Moulas et al., 2014). Understanding the impact of heterogeneous rock deformation on (de)hydration reactions is, hence, essential to unravel the interplay between lithosphere deformation and (de)hydration reactions.

A method to quantify the interplay between lithosphere deformation, fluid flow and metamorphic reactions is mathematical modelling. A particular challenge for such models is the significantly different temporal and spatial scales of fluid flow and viscous flow of the lithospheric rocks (e.g. Quinquis and Buiter, 2014). Therefore, many numerical models focussing on lithosphere deformation employ significantly simplified models to quantify fluid flow and/or reactions (e.g. Quinquis and Buiter, 2014). For example, in some earlier models, the magnitude and direction of fluid velocity are prescribed to a constant value (e.g. Gerya et al., 2008). In other models, the fluid velocity is described by a Darcy-type law, but it is assumed that the fluid pressure is equal to the rock pressure (e.g. Yang and Faccenda, 2020). In contrast to such lithospheric-scale models, two-phase models can calculate both solid deformation and fluid flow, based on a self-consistent system of governing equations (e.g. Biot, 1941; Malvoisin et al., 2015; Yarushina and Podladchikov, 2015; Evans et al., 2020). However, many of these models are currently still assuming that solid deformation is negligible and set the solid velocities to zero (e.g. Plümper et al., 2017; Beinlich et al., 2020).

Other models focus on homogeneous deformation and ignore shear deformation or mechanical heterogeneities (e.g. Brantut et al., 2011; Malvoisin et al., 2015).

Here, we aim to take a further step toward quantifying the interplay between heterogeneous rock deformation, fluid flow and metamorphic reactions. We study the impact of volumetric and shear deformation in a mechanically heterogeneous, poroviscous medium on fluid flow and (de)hydration reactions. Our two-dimensional (2D) mathematical model for hydro-mechanical-chemical (HMC) two-phase processes extends the model of Malvoisin et al. (2015). The mechanical part of our HMC model can calculate stress and pressure variations around mechanically weak inclusions in a compressible power-law viscous medium under far-field pure-shear shortening. We study the deformation of a medium with weak elliptical inclusions because such model captures the first-order stress and deformation features of weak lithospheric shear zones (Moulas et al., 2014). The hydro-chemical part of the model can calculate the evolution of fluid pressure, porosity and solid as well as fluid densities including (de)hydration reactions. Although our HMC model is generally applicable, for transparency and clarity, we apply the model here to a simple brucite ($Mg(OH)_2$) – periclase (MgO) – water (H_2O) system (Fig. 1). We also chose the brucite – periclase (de)hydration reaction, because it can involve considerable volume and porosity changes (e.g. Carmichael, 1987; Zheng et al., 2018) and is, hence, a good test for the numerical robustness of our HMC model. For simplicity, we assume a constant temperature and a constant system composition (closed system), and we assume that solid and fluid densities are only a function of the fluid pressure.

The aims of our study are: (1) to present a self-consistent system of equations to quantify (de)hydration reactions and fluid flow in mechanically heterogeneous and deforming poroviscous rock, (2) to present a numerical pseudo-transient finite-difference algorithm to solve the system of equations, (3) to quantify the impact of volumetric and shear deformation

157 on the brucite-periclase (de)hydration reaction and the evolving reaction front, (4) to quantify
158 differences between fluid and rock pressure, and between fluid and solid velocities, and (5) to
159 quantify the reaction-induced rheological weakening of the modelled heterogeneous rock.

160

161 **2. Mathematical model**

162 *2.1. Porous medium densities for the brucite, periclase and water system*

163 We consider a porous medium, with porosity ϕ, which consists of a solid phase with
164 density ρ_s and a pore fluid with density ρ_f so that the total density of the porous medium is

165 $$\rho_T = \rho_f \phi + \rho_s (1-\phi). \quad (1)$$

166 We assume that the solid phase consists of two components, (1) a non-volatile component that
167 remains in the solid and (2) a volatile component that is liberated during dehydration. For the
168 considered brucite-periclase system, the non-volatile component is MgO, and the volatile
169 component is H_2O. To quantify the non-volatile component of MgO in the solid phase, we use
170 its mass (in kg) fraction, X_s. Periclase has a molar mass of 0.0403 kg/mol, water of 0.0180
171 kg/mol and brucite of 0.0583 kg/mol. Therefore, we set $X_s = 1$ for periclase and $X_s = 0.69$
172 for brucite. Furthermore, we define the relative density of the solid component in the solid
173 phase as

174 $$\rho_X = \rho_s X_s \quad (2)$$

175 *2.2. Hydro-chemical model*

176 The conservation of total mass is described by

177 $$\frac{\partial \rho_T}{\partial t} + \nabla \left[\rho_f \phi \mathbf{v}^f + \rho_s (1-\phi) \mathbf{v}^s \right] = 0 \quad (3)$$

where t is time, ∇ is the divergence operator and $\mathbf{v}^f$ and $\mathbf{v}^s$ are vectors of the fluid and solid (barycentric) velocities, respectively. For vector and tensor quantities, we use indices f and s as superscripts, because vector and tensor components will have additional subscripts indicating the spatial direction, and scalar quantities can be easier distinguished from vector and tensor quantities. We modify equation (3) by subtracting and adding $\mathbf{v}^s$ to $\mathbf{v}^f$, yielding

$$\frac{\partial \rho_T}{\partial t} + \nabla\left[\rho_f \phi\left(\mathbf{v}^f - \mathbf{v}^s + \mathbf{v}^s\right) + \rho_s\left(1-\phi\right)\mathbf{v}^s\right] = 0 \tag{4}$$

and then to re-group the velocity vectors with the total density, ρ_T, to yield

$$\frac{\partial \rho_T}{\partial t} + \nabla\left[\rho_f \phi\left(\mathbf{v}^f - \mathbf{v}^s\right)\right] + \nabla\left(\rho_T \mathbf{v}^s\right) = 0\,. \tag{5}$$

Now, the relative velocity of the fluid to the solid, $\mathbf{v}^f - \mathbf{v}^s$, can be expressed by Darcy's law in the absence of gravity

$$\phi\left(\mathbf{v}^f - \mathbf{v}^s\right) = -\frac{k\phi^3}{\eta_f}\nabla p_f \tag{6}$$

where k and η_f are the permeability coefficient in a Kozeny–Carman-type permeability expression and the fluid viscosity, respectively. Similar to total mass, the conservation of the total non-volatile component (MgO) is described by

$$\frac{\partial}{\partial t}\left[\rho_X\left(1-\phi\right)\right] + \nabla\left[\rho_X\left(1-\phi\right)\mathbf{v}^s\right] = 0\,. \tag{7}$$

There is no fluid velocity in this conservation equation because we assume that the dissolution of MgO in the fluid is negligible.

We assume a constant temperature and a closed system with constant system composition so that we have equal molar amounts of H_2O and MgO. Our system has a

constant composition as a whole, but its composition can vary locally because of local mass exchange (e.g. reaction and/or diffusion). We approximate ρ_s, ρ_f and X_s as a function of p_f, which can be expressed as

$$\begin{aligned} \rho_f &= \rho_f\left(p_f\right) \\ \rho_s &= \rho_s\left(p_f\right) \\ X_s &= X_s\left(p_f\right) \end{aligned} \quad . \tag{8}$$

The values of ρ_s, ρ_f and X_s for a range of values of p_f are calculated by Gibbs free-energy minimization (e.g. Connolly, 2005; Fig. 1), using the thermodynamic dataset of Holland and Powell (1998).

2.3. Mechanical model

We consider a 2D viscous material, which represents the solid part of the poroviscous medium. We employ a power-law viscous flow law, which is typically applied to model dislocation creep (e.g. Gerya, 2019). The relations between the deviatoric stress tensor components, $\tau_{ij} = \sigma_{ij} + p\delta_{ij}$ (where σ_{ij} are the components of the total stress tensor, p is total pressure and δ_{ij} is the Kronecker delta) and solid velocity gradients, or deviatoric strain rate tensor components D_{ij}, are (e.g. Schmalholz and Schmid, 2012)

$$\tau_{ij} = 2\eta^s \left(\frac{\tau_{II}}{\tau_{ref}} \right)^{1-n} D_{ij} \tag{9}.$$

where subscripts i and j are either 1 (representing the horizontal x-direction) or 2 (representing the vertical y-direction), η^s is the solid shear viscosity, τ_{II} is the square root of the second invariant of the deviatoric stress tensor, $\tau_{II} = \sqrt{\tau_{xx}^2 + \tau_{xy}^2}$, τ_{ref} is a reference stress, n is the stress exponent and $D_{ij} = \left(\partial v_i^s / \partial x_j + \partial v_j^s / \partial x_i\right)/2 - \delta_{ij}\left(\partial v_i^s / \partial x_i\right)/3$. For $n = 1$, the

material is linear viscous having a constant viscosity η^s. For simplicity, we also consider a viscous volumetric deformation for which the divergence of the solid velocity field is related to the difference between total pressure, p, and fluid pressure, p_f (e.g. Yarushina and Podladchikov, 2015)

$$\nabla \mathbf{v}^s = -\frac{p - p_f}{(1-\phi)\lambda} \tag{10}$$

where λ is the bulk viscosity. The applied force balance equations without inertial forces and gravity are

$$\nabla \sigma_{ij} = 0 \tag{11}.$$

2.4. Governing system of equations

The above equations represent a system of 11 equations for 11 unknowns, which are p_f, ϕ, ρ_s, ρ_f, X_s, p, v_x^s, v_y^s, τ_{xx}, τ_{yy} and τ_{xy}, assuming that the deviatoric stress tensor is symmetric, $\tau_{xy} = \tau_{yx}$. The three deviatoric stress tensor components are calculated using the three flow law equations (9). The solid pressure is determined from the bulk-flow law, equation (10). The solid and fluid densities and the mass fraction are calculated by the three pre-computed thermodynamic data tables (equation (8) and Fig. 1C and D). Equation (5) is used to determine the fluid pressure, p_f, equation (7) to determine the porosity, ϕ, and the two force balance equations (11) to determine the two solid velocities, v_x^s and v_y^s. To determine p_f, ϕ, v_x^s and v_y^s we use an iterative numerical method, here referred to as pseudo-transient (PT) method (e.g. Chorin, 1968; Duretz et al., 2019; Räss et al., 2019). Therefore, we add a pseudo time derivative of the unknown variables p_f, ϕ, v_x^s and v_y^s to the

corresponding equations, which we use to determine these variables. The pseudo-transient equations are

$$\begin{aligned}
\frac{\partial^{PT} p_f}{\partial t_{pf}^{PT}} &= -\frac{\partial \rho_T}{\partial t} + \nabla\left[\rho_f \frac{k\phi^3}{\eta_f}\nabla p_f\right] - \nabla\left(\rho_T \mathbf{v}^s\right) \\
\frac{\partial^{PT} \phi}{\partial t_{\varphi}^{PT}} &= \frac{\partial}{\partial t}\left[\rho_X\left(1-\phi\right)\right] + \nabla\left[\rho_X\left(1-\phi\right)\mathbf{v}^s\right] \quad . \\
\frac{\partial^{PT} v_i^s}{\partial t_v^{PT}} &= \nabla\sigma_{ij}
\end{aligned} \tag{12}$$

When the PT time derivatives of the left-hand sides of the equations (12) are zero, then the corresponding steady-state equations are solved. The closed system of governing equations is given by equations (8), (9), (10) and (12). Model variables and parameters are given in table 1.

2.5. Model configuration

We present the model configuration before presenting the numerical method because some of the numerical parameters, such as the numerical time step, depend on the model configuration (Fig. 2). It is essential to apply physically consistent initial conditions. Hence, we first assume ambient conditions for which the unknown parameters are constant in the 2D model domain. We then apply an initial perturbation for p_f in a circular, or elliptical, region in the center of the model domain (Fig. 3). This perturbation either increases or decreases the ambient value of p_f. We consider two initial configurations: (1) ambient conditions for which periclase and water are stable with a positive fluid-pressure perturbation generating locally higher fluid pressures inside the inclusion for which brucite is stable; (2) ambient conditions for which brucite is stable and a negative pressure perturbation for which locally periclase and water are stable. The initial porosity field, ϕ_0, must be consistent with the applied initial fluid pressure field including a pressure perturbation. The initial porosity is

$$\phi^0 = 1 - \frac{\rho_X^{amb}\left(1-\phi^{amb}\right)}{\rho_X^0} \tag{13}$$

where ρ_X^{amb} is the corresponding density for the applied ambient fluid pressure, ϕ^{amb} is the initially ambient porosity and ρ_X^0 is the initial density field for the initial fluid-pressure field including the perturbation. Equation (13) shows that ϕ_0 cannot be constant initially if a fluid pressure perturbation is applied because ρ_X^0 varies according to the applied fluid pressure perturbation. Equation (13) is derived from equation (7), assuming zero solid velocities. To guarantee that ϕ_0 is initially everywhere positive requires according to equation (13) that $\phi^{amb} > 1 - \rho_X^0 / \rho_X^{amb}$. Boundary conditions for p_f and ϕ are of Dirichlet type, and boundary values are fixed to the initial ambient values.

We also show simulations for a configuration with inclusions, which have a smaller shear viscosity than the surrounding (Figs. 5 to 9). Furthermore, we show simulations for far-field pure-shear shortening boundary conditions, with horizontal shortening and vertical extension, so that the divergence of the applied boundary velocity field is zero (Figs. 5 to 9). We assume a constant temperature of 800 °C (Fig. 1).

2.6. Numerical algorithm and dimensionless parameters

All derivatives are approximated with discrete difference ratios following the standard procedure of staggered finite difference (FD) methods (e.g. Gerya, 2019). The numerical algorithm consists of a standard time loop with an internal PT iteration loop. During this PT iteration loop, the PT time derivatives in the discretized equations (12) approach zero. In practice, we iterate until the PT time derivative becomes smaller than a specified numerical tolerance error. Approximating the time derivatives with the FD method generally requires four numerical time steps, which are the physical time step, Δt, controlling time evolution,

the PT time step to solve for p_f, Δt_{pf}^{PT}, the PT time step for ϕ, Δt_{φ}^{PT}, and the PT time step for v_x^s and v_y^s, Δt_v^{PT}. The choice of the numerical time steps is crucial for a stable convergence of the PT iterative solution, but the time steps do not affect the result after convergence. For the presented simulations, we employed the following numerical time steps:

$$
\begin{aligned}
\Delta t &= 2\frac{r^2\eta_f}{k\,\beta_{eff}} \\
\Delta t_{pf}^{PT} &= \frac{1}{16}\frac{\max\left(\Delta x,\Delta y\right)^2}{\max\left(\dfrac{k\,\phi^3}{\beta_{eff}}\right)} \\
\Delta t_{\phi}^{PT} &= \Delta t \\
\Delta t_{v}^{PT} &= \frac{1}{16}\frac{\max\left(\Delta x,\Delta y\right)^2}{\max\left(\eta^s\right)}
\end{aligned}
\qquad (14).
$$

where $\beta_{eff} = 0.01/\,p_{ini}$, r is the inclusion radius (the small radius in case of an elliptical inclusion), Δx and Δy are horizontal and vertical grid spacing, respectively, and p_{ini} is the initial value of the ambient fluid pressure. There are many possibilities to scale and/or non-dimensionalize the model parameters inside the numerical algorithm. We programmed the numerical algorithm in such a way that the specific magnitudes of individual parameters, such as shear viscosity, are not significant and the characteristic physical behaviour of the system is controlled by dimensionless parameters. This scaling provided the most stable convergence during the PT iterations. The dimensionless parameters and numerical examples applied in the simulations are:

$$
\begin{aligned}
&\Gamma_1 = \frac{w}{r} && e.g.\quad \Gamma_1 = \frac{10^{-1} m}{10^{-2} m} = 10 \\
&\Gamma_2 = \frac{k}{\eta_f}\frac{\eta^s}{r^2} && e.g.\quad \Gamma_2 = \frac{10^{-19} m^2}{10^{-3} Pas}\frac{10^{20} Pas}{\left(10^{-2} m\right)^2} = 10^8 \\
&\Gamma_3 = \frac{\lambda}{\eta^s} && e.g.\quad \Gamma_3 = \frac{10^{20} Pas}{10^{20} Pas} = 1 \\
&\Gamma_4 = \frac{\bar{D}_{xx}\eta^s}{p_{ini}} && e.g.\quad \Gamma_4 = \frac{2\times10^{-14} s^{-1} 10^{20} Pas}{8.5\times10^8 Pa} = 0.0024 \\
&\Gamma_5 = \frac{\tau_{ref}}{p_{ini}} && e.g.\quad \Gamma_5 = \frac{2.5\times10^7 Pa}{8.5\times10^8 Pa} = 0.024
\end{aligned}
\tag{15}
$$

where w is the model width and $\bar{D}_{xx}$ is the applied far-field horizontal pure-shear shortening rate. We model purely mechanical, M, (fluid velocity is zero, no reactions), purely hydro-chemical, HC, (solid velocity is zero) and fully coupled hydro-mechanical chemical, HMC, systems. Parameter Γ_1 applies to all systems, parameter Γ_2 to HC systems and parameters Γ_3, Γ_4 and Γ_5 to HMC systems, where Γ_4 controls the far-field deformation via $\bar{D}_{xx}$ and Γ_5 only applies for power-law viscous deformation, $n > 1$.

The shear viscosity of the inclusion can be different from the one of the surrounding medium. The initial inclusion boundary represents the reaction boundary between brucite and periclase. This boundary will move during the simulations with progressive fluid pressure diffusion. Hence, also the boundary between regions of high porosity (periclase and water region) and low porosity will move. The boundary between brucite and periclase is controlled by a considerable change in porosity. Therefore, we define the brucite-periclase boundary by the average porosity between the brucite and periclase-water region. The brucite-periclase reaction boundary evolves, hence, together with the evolving porosity field. At each time step, the shear viscosity distribution is adjusted in order to coincide with the evolving reaction boundary. Therefore, the size and geometry of the mechanically weaker inclusion are changing as time progresses.

We programmed the numerical algorithm in MATLAB. We provide the entire algorithm for the most complex HMC model configuration, which is online available under: https://github.com/schmaste/HMC_Brucite.

3. Results

We present first results of a mechanical (M) model to test the applicability of the PTFD method to calculate pressure variations around weak inclusions for far-field shortening (e.g. Schmid and Podladchikov, 2003; Moulas et al., 2014). To test our algorithm further, we show results of a HC model to reproduce the overall results for nonlinear diffusion of fluid pressure perturbations (Malvoisin et al., 2015). Finally, we present fully coupled HMC models to test the impact of far-field deformation and mechanical heterogeneities on fluid flow and reaction-front evolution.

3.1. Heterogeneous mechanical model

A weak circular inclusion is embedded in a linear viscous medium under horizontal pure-shear shortening (Figs. 2 and 3A and B). The relevant dimensionless parameters are $\Gamma_1 = 14$, $\Gamma_3 = 1$ and $\Gamma_4 = 0.0024$. We also consider an elliptical inclusion (Fig. 3C and D). The aspect ratio of the ellipse is three, and the long axis is tilted 30° to the vertical direction. The relevant dimensionless parameters are $\Gamma_1 = 14$ (where the radius corresponds to the short axis of the ellipse), $\Gamma_3 = 1$ and $\Gamma_4 = 0.0024$. Inside the circular and elliptical inclusion, η^s is a factor 1000 smaller than in the surrounding medium. We calculate the distributions of p and compare them with the corresponding analytical solutions from Moulas et al. (2014). The results show that the applied PTFD algorithm with a staggered Eulerian grid can calculate the characteristic pressure variations around the weak inclusions under far-field shortening (Fig.

333 3). The numerical and analytical solutions are not fully comparable because (1) the analytical
334 solution considers incompressible deformation while the numerical algorithm considers
335 viscous volumetric deformation, and (2) the analytical solution applies to an infinite domain
336 while in the numerical model the pure-shear boundary conditions are applied at the
337 boundaries of the finite model domain. However, the numerical and analytical solutions show
338 similar magnitudes and distribution of p.

339 *3.2. Hydro-Chemical model*

340 We consider a porous medium without solid deformation and set the solid velocities to
341 zero. Initially, the ambient fluid pressure and porosity are perturbed within a circular domain
342 (Fig. 4). This domain has the same viscosity as the surrounding and the model is mechanically
343 homogeneous. We apply the parameters $\Gamma_1 = 10$ and $\Gamma_2 = 10^8$.

344 First, we apply an initially higher fluid pressure in the circular region so that initially
345 brucite is stable inside the inclusion and periclase is stable outside the inclusion. The initial
346 ambient value of $p_f = p_{ini} = 6.5$ kbar and in the inclusion $p_f = 8.45$ kbar. The ambient initial
347 $\phi = 0.55$ and in the inclusion $\phi = 0.007$. We chose this porosity distribution to test the
348 algorithm in the limit of low porosity. Figure 4 shows horizontal profiles of p_f and ϕ in the
349 left model half and the vertical model center. The configuration corresponds to models of
350 Malvoisin et al. (2015) for reactions with positive Clapeyron slope (their figure 10E and F).
351 With progressive time, the initially step-like perturbation of p_f is diffusing while the profile
352 of ϕ maintains a step-like shape representing the motion of a dehydration front, that is a front
353 indicating the release of water from brucite (Fig. 4A and B). Once values of p_f drop below
354 7.85 kbar, which is the value that defines the reaction from brucite to periclase, no brucite is
355 present anymore in the model, which is indicated by constant $\phi = 0.55$.

Second, we apply an initially smaller fluid pressure in the circular region so that initially periclase is stable inside the inclusion and brucite outside the inclusion. At first, the ambient value of $p_f = 8.5$ kbar and inside the inclusion $p_f = 6.8$ kbar. The ambient initial $\phi = 0.001$ and in the inclusion $\phi = 0.55$, again to test the algorithm in the limit of low porosity. This configuration corresponds to models shown in figure 10G and H of Malvoisin et al. (2015). With progressive time, the step-like perturbation of p_f is diffusing, but the profile of p_f maintains a sharp front above the fluid pressure of 7.85 kbar, which is the pressure at the reaction from brucite to periclase (Fig. 1C and D). The profile of ϕ also maintains a step-like shape representing the motion of a dehydration front, which moves outward toward the brucite region (Fig. 4C and D).

3.3. Hydro-Mechanical-Chemical model

We consider the full HMC model to investigate the impact of solid deformation and mechanical heterogeneity on the evolution of p_f and ϕ, and on the reaction front evolution. We consider linear viscous deformation and perform five models with increasing deformation complexity (Fig. 5). The models include a circular ($\Gamma_1 = 10$) or elliptical inclusion with a vertical radius two or three times larger than the horizontal radius, for which $\Gamma_1 = 10$. In the inclusions, the fluid pressure ($p_f = 6.5$ kbar) is initially smaller than the outside ambient pressure ($p_f = 8.5$ kbar). For all models, $\Gamma_2 = 10^8$ and $\Gamma_3 = 1$, except that η^s inside the inclusion is a factor 1000 smaller than outside. We assume that the effective shear viscosity of the high-porosity, poroviscous periclase-water region is much smaller than the effective viscosity of the low-porosity brucite region and, hence, apply a smaller shear viscosity inside the inclusion. The first HMC model has a circular inclusion and no far-field deformation ($\Gamma_4 = 0$; Fig. 5B), the second model has a circular inclusion and far-field deformation (

379 $\Gamma_4 = 0.0024$; Fig. 5C), the third model has an elliptical inclusion with aspect ratio of two and
380 far-field deformation (result only shown in Fig. 6), and the fourth model has an elliptical
381 inclusion with aspect ratio of three and far-field deformation ($\Gamma_4 = 0.0024$; Fig. 5D). For
382 comparison, we also show the corresponding HC model, for which solid velocities are zero
383 (Fig. 5A).

384 In all models, the stability field of periclase, and the associated high-porosity region, is
385 growing with time due to diffusion of p_f (e.g. Fig. 5). In the HMC model without far-field
386 deformation, the solid velocities indicate a radially symmetric contraction of the solid (Fig.
387 5B). The direction of solid and fluid velocities is essentially identical. In the HMC model with
388 circular inclusion and far-field deformation, away from the circular inclusion, the solid
389 velocities indicate the applied horizontal shortening and vertical extension (Fig. 5C). Around
390 the inclusion, the solid velocities change direction and show a radial contraction. Inside the
391 inclusion, the directions of solid and fluid velocities are different. In the HMC model with far-
392 field deformation and elliptical inclusion, the solid velocities indicate horizontal shortening
393 and vertical extension, and around the inclusion contraction (Fig. 5D). Inside the inclusion,
394 the directions of solid and fluid velocities are different. For all HMC models, the maximal
395 fluid velocities are approximately seven orders of magnitudes larger than the solid velocities
396 (see also Fig. 7D and E). The order of magnitude of the fluid velocity can be estimated from
397 equation (6). Based on the applied parameters (equation (15)), assuming no solid velocity, a
398 fluid-pressure gradient of 2 kbar/cm and a representative porosity of 0.1 yields 2×10^{-8} m/s.
399 For the HMC models with far-field deformation, the shortening velocity is the product of
400 shortening rate and half-model width, which yields according to the values in equation (15) a
401 solid velocity of 10^{-15} m/s.

With progressive time, the horizontal profiles, in the vertical model middle, of p_f and ϕ differ for the five models (Fig. 6). Profiles of p_f and ϕ are similar for the two HMC models with circular inclusion, indicating that far-field deformation does not significantly affect the evolution of p_f and ϕ. However, profiles of p_f and ϕ are different for the HMC models with elliptical inclusions and show a broader region with periclase and, hence, a more displaced dehydration front. The width of the periclase region in the HC model is similar to the width in the two HMC models with circular inclusions, whereas p_f has diffused slightly less for the two HMC models. The similar width of the periclase region for the HC and HMC models with circular inclusion shows that solid deformation has a minor impact on the propagation of the dehydration front for the applied configuration. The reason is that circular inclusions under far-field deformation do not generate a perturbation in p with respect to the far-field value of p (e.g. Moulas et al., 2014). This is different for weak elliptical inclusions with the long axis orthogonal to the shortening direction, as applied here, which exhibit higher p inside the inclusion compared to the far-field value (e.g. Moulas et al., 2014). For circular and elliptical inclusions, the distribution of p inside the inclusion is homogeneous (e.g. Moulas et al., 2014). The higher p inside elliptical inclusions causes a higher p_f, with respect to circular inclusions, and, hence, a wider diffusion region (Fig. 7). Furthermore, values of p inside elliptical inclusions are larger for higher aspect ratios, which explains why the elliptical inclusion with an aspect ratio of 3 has a broader diffusion region than the inclusion with an aspect ratio of 2 (Fig. 6).

With progressive time, p_f diffuses fastest for the two HMC models with circular inclusion and slowest for the HMC model with an elliptical inclusion of aspect ratio three (Fig. 6C). For all models, diffusion of p_f is fastest during the initial stage of the simulations

and progressively slows down significantly (Fig. 6C). The diffusion of p_f controls the displacement of the dehydration front, which shows a similar nonlinear time evolution as p_f (Fig. 6D). The dehydration front in the HMC model with elliptical inclusion of aspect ratio three moves fastest whereas the dehydration front for the HMC models with circular inclusion moves slowest. For the applied parameters, the dehydration front has moved a distance between $r/2$ (i.e. 0.5 cm) and r within 220 hours (9.2 days). The results show that deformation of a mechanically heterogeneous medium has an impact on the evolution of fluid pressure and of the reaction front, which depends on the geometry of the heterogeneity.

The model domain represents a deforming, heterogeneous rock in which a dehydration reaction occurs. The effective viscosity of the heterogeneous rock, $\bar{\eta}$, can be calculated by the ratio of $\langle \tau_{II} \rangle / 2\bar{D}_{xx}$, where $\langle \tau_{II} \rangle$ is the area-averaged value of τ_{II} and $\bar{D}_{xx}$ represents the second invariant of the deviatric strain rate tensor corresponding to the applied bulk pure-shear deformation of the model domain, which is constant throughout the simulations. The progressive dehydration reaction decreases the value of $\bar{\eta}$ with progressive deformation because the surface of the weak inclusion increases and the stress field changes (Fig. 7A and D). The decrease of $\bar{\eta}$ with progressive reaction and deformation represents a reaction-induced weakening of the heterogeneous rock. The weakening is fastest at the beginning of deformation and subsequently slows down significantly. This overall weakening evolution is linked to the evolution of the inclusion surface (Fig. 7D) which grows fastest at the beginning of the simulation and then subsequently slows down. However, the magnitude of the weakening, here between 30% and 50% effective viscosity reduction (Fig. 7A), depends on the inclusion shape, and elliptical inclusions with larger aspect ratio exhibit more weakening (Fig. 7A). For comparison, we also show the evolution of the harmonic average, or mean, and of the arithmetic average of the viscosity fields (Fig. 7B and C). The simulations employ a

449 linear shear viscosity and, therefore, the evolution of the harmonic and arithmetic mean of the
450 viscosity field depends only on the relative inclusion surface inside the model domain. The
451 results show a strongly non-linear weakening with time and, hence, with progressive bulk
452 strain since the applied bulk far-field pure-shear strain rate is constant.

453 To illustrate all features of our HMC model, we present results of a simulation with an
454 oblique elliptical inclusion and a power-law viscous medium (Figs. 8 and 9). The long axis of
455 the elliptical inclusion forms a 60° angle with the horizontal shortening direction. The applied
456 dimensionless parameters are $\Gamma_1 = 10$, $\Gamma_2 = 10^8$, $\Gamma_3 = 1$, $\Gamma_4 = 0.0024$, $\Gamma_5 = 0.024$ and $n = 3$.
457 Results are made dimensional with the example values used in equation (15). Magnitudes of
458 p and p_f are significantly different both inside and outside the inclusion (Fig. 8A and B).
459 While p is homogeneous inside the inclusion and varies outside, p_f, in contrast, varies
460 inside the inclusion but is homogeneous outside. The divergence of the solid velocity, $\nabla\left(\mathbf{v}^s\right)$,
461 shows contraction (negative values) inside the inclusion but mainly expansion (positive
462 values) outside the inclusion (Fig. 8C). The distribution of the absolute magnitude of the fluid
463 velocity, $\left|\mathbf{v}^f\right| = \sqrt{\left(v_x^f\right)^2 + \left(v_y^f\right)^2}$, indicates that fluid flow only occurs inside the inclusion,
464 where ϕ is large and where there is a gradient of p_f (Fig. 8D). The absolute magnitude of the
465 solid velocity, $\left|\mathbf{v}^s\right| = \sqrt{\left(v_x^s\right)^2 + \left(v_y^s\right)^2}$, shows that solid deformation is significant inside and
466 outside the inclusion (Fig. 8E). The magnitudes of absolute solid and fluid velocities indicate
467 that fluid velocities, as estimated above, are approximately seven orders of magnitude larger
468 than the solid velocities. For illustration, we also calculate approximate fluid velocities by
469 using p instead of p_f in the Darcy equation (6). These approximate fluid velocities are zero
470 inside the inclusion since p is homogeneous (Fig. 8F). Hence, fluid velocities calculated with
471 rock pressure gradients can be considerably different from the fluid velocities calculated with

fluid pressure gradients (Fig. 8D and F). The distribution of the shear stress, τ_{xy}, is homogenous inside the inclusion and varies outside (Fig. 8G). For the applied parameters, the largest magnitudes of τ_{xy} are in the order of 40 MPa. Also, τ_{II} is homogeneous inside the inclusion and varies only outside (Fig. 8H), which is the reason why the effective, stress-dependent shear viscosity of the solid, η^s, varies only outside the inclusion (Fig. 8I). An enlargement of the model domain shows that the current inclusion boundary, representing the dehydration front, defines the transition from contraction inside the inclusion to expansion outside (Fig. 9A). The applied far-field pure-shear, with horizontal shortening and vertical extension, would generate a zero divergence of the solid velocity, $\nabla \mathbf{v}^s$. Values of $\nabla \mathbf{v}^s$ are mostly positive outside the inclusion, indicating expansion, showing that the contraction inside the inclusion generates an expansion outside the inclusion to conserve total volume (Fig. 9A), which is imposed by the volume conserving, pure-shear boundary conditions. For the presented results, we consider a pure-shear far-field shortening rate, $\bar{D}_{xx}$, of 2×10^{-14} s^{-1} (equation (15)). Maximal magnitudes of $\nabla \mathbf{v}^s$ are in the order of -1×10^{-12} s^{-1} showing that contraction rates are approximately two orders of magnitudes faster than the applied far-field shortening rates (Fig. 9A). Fluid and solid velocities parallel to the short axis of the ellipse are significantly faster than the velocities parallel to the long axis (Fig. 9B and C). Both magnitudes and directions of solid and fluid velocities are different inside the inclusion (Fig. 9B and C).

4. Discussion

In the discretized PT mass conservation equation (12), we keep the products of velocity, density and porosity within the divergence term. We do not "open" the divergence term to obtain separate advection terms, for example, products of velocity multiplied by

density gradient. Although we did not compare different numerical discretization schemes, we suggest that the applied conservative numerical scheme in fully divergent form is useful for numerical stability during modelling the propagation of sharp porosity and dehydration fronts, such as shown in figures 4 and 6. To test the numerical convergence of the algorithm, we performed the simulation for the most complex HMC model (Figs. 8 and 9) for different numerical resolutions (Fig. 10). We run simulations with resolutions of 31×31, 51×51, 101×101, 151×151, 201×201, 301×301 and 401×401 grid points until a time corresponding to 3.3 hours. The distribution of p_f (Fig. 10A to C) and $\left|\mathbf{v}^s\right|$ (Fig. 10D to F) does not show numerical oscillations around the dehydration front; the numerically calculated fields of p_f and $\left|\mathbf{v}^s\right|$ have not been smoothed during the simulations. The minimal value of p_f at the end of each simulation varies for the different numerical resolutions but varies less and less with increasing resolution indicating the numerical convergence (Fig. 10G). Similarly, the maximal value of $\left|\mathbf{v}^s\right|$ at the end of each simulation varies less and less with increasing resolution (Fig. 10G). The numerical results and convergence test indicate that the PTFD algorithm is suitable to numerical simulate the coupling of heterogeneous rock deformation, porous fluid flow and metamorphic reactions involving the propagation of sharp porosity and reaction fronts.

We consider a simple metamorphic reaction to investigate the fundamental impact of deformation in a heterogeneous solid on the reaction and fluid flow. It is, in principle, straightforward to extend the model to more complicated reactions involving more components, such as presented in Malvoisin et al. (2015). We assumed that the solid density is a function of the fluid pressure (equation (8)). Although for pure isotropic solids the density variations are a consequence of mean-stress variations (see Moulas et al., 2019, for discussion), it has been experimentally demonstrated that dehydration reactions are controlled by fluid pressure (e.g. Llana-Fúnez et al., 2012). When solid-fluid interactions are considered,

520 the mean stress of the solid grains may not be the most appropriate macroscopic
521 thermodynamic variable to quantify metamorphic phase equilibrium (e.g. Dahlen, 1992; see
522 also discussion in Schmalholz and Podladchikov, 2014). For solid-fluid interactions, mineral
523 devolatilization reactions must be investigated at the respective solid-fluid interface (e.g.
524 Dahlen, 1992). However, our mathematical model constitutes a two-phase, or a superposed
525 two-field, solid-fluid continuum, in which the solid-fluid interfaces are not resolved.
526 Therefore, we need to approximate the thermodynamic pressure by some model quantity. For
527 the (de)hydration reaction, the variation of total density is much larger than the density
528 variation of the solid minerals. Therefore, the porosity evolution caused by the (de)hydration
529 reactions controls the overall total density variation, and consequently, the volumetric
530 deformation of the solid. Hence, we apply the fluid pressure as most appropriate proxy for the
531 macroscopic thermodynamic pressure.

532 We model a closed system in equilibrium, and assume that the transport of the hydrous
533 fluid occurs by porous flow. Therefore, all the hydrous fluid required for the reaction is
534 already in the system. Consequently, the reaction from periclase and H_2O-pure fluid to brucite
535 decreases the volume of the system, because the fluid in the pore space is bounded after the
536 reaction in the brucite and porosity is significantly reduced. In an open system, the hydration
537 of periclase, at pressure and temperature where brucite can form in the presence of water,
538 generates a total-volume increase because water is added to the system during the reaction.
539 Such hydration can cause reaction-induced fracturing in the rocks surrounding the hydrating
540 periclase (e.g. Carmichael, 1987; Kuleci et al., 2017).

541 Our model configuration and results may be applicable to reactions related to fluid
542 transfer inside and across shear zones. Moulas et al. (2014) showed that mathematical models
543 of weak inclusions in viscous medium capture the first-order mechanical response of shear
544 zones that develop in 2D visco-elasto-plastic thermo-mechanical numerical models during

lithosphere shortening (e.g. Schmalholz and Podladchikov, 2013; Jaquet and Schmalholz, 2018). Fluid transfer and associated reactions are likely important during shear zone formation because the fluid enables reactions whose products can be weaker than the protolith (e.g. Jolivet et al. 2005). Therefore, fluid-driven mineral reactions can cause weakening during shear zone evolution, as was suggested for the fluid-controlled transformation from granulite to eclogite (e.g. Austrheim, 1987; Jamtveit et al., 2000; Jolivet et al. 2005). Due to the weakening, shear zones exhibit smaller effective viscosities and deviatoric stresses than the surrounding wall rock and can, hence, exhibit different fluid and solid pressures compared to the less-deforming wall rock (e.g. Schmalholz and Podladchikov, 2013; Jamtveit et al., 2018). Our model may be, hence, useful to study fluid transfer and reactions in shear zones. Furthermore, our models show that reaction-induced weakening in a heterogeneous rock is strongly nonlinear with progressive time and, hence, progressive strain. Weakening is strongest during the initial stages of the reaction because it is controlled by fluid-pressure diffusion, which is controlled by the decreasing fluid pressure gradients. Also, significant reaction-induced weakening may occur within a small amount of strain because the fluid velocities, controlling reaction-front propagation, may typically be significantly faster than the solid velocities during tectonic deformation.

5. Conclusions

The presented 2D hydro-mechanical-chemical model and the applied pseudo-transient finite difference numerical algorithm are suitable to quantify the interplay between metamorphic reactions and fluid flow in a deforming, heterogeneous, poroviscous medium. The medium is mechanically heterogeneous, because the mineral-fluid asemblages involved in the reaction have different effective viscosities. Our model can simulate the power-law viscous deformation of a heterogeneous medium coupled to Darcy-type porous fluid flow,

570 whereby solid and fluid velocities differ by seven orders of magnitude. Furthermore, the
571 model can simulate the propagation of a sharp, step-like, (de)hydration, porosity and viscosity
572 front.

573 Our results show that rock deformation and mechanical heterogeneities can have a
574 considerable impact on fluid flow and metamorphic reactions because heterogeneities in
575 deforming rock can cause rock pressure variations, which in turn cause fluid pressure
576 variations that impact the reaction. In the simulations, the propagation of the reaction front
577 during deformation causes a reaction-induced weakening of the heterogeneous rock because
578 the surface of a weak mineral-fluid assemblage increases due to the reaction. This reaction-
579 induced weakening is controlled by fluid-pressure diffusion and is strongly nonlinear with
580 progressive strain, whereby weakening is most significant during the initial stages of the
581 reaction. Also, in deforming heterogeneous rock, magnitudes, gradients and distributions of
582 fluid pressure and rock pressure can be significantly different so that also directions of fluid
583 and solid velocities can be different. Therefore, models calculating fluid velocities from
584 gradients of the rock pressure are likely considerably inaccurate if applied to deforming
585 heterogeneous rock, such as in and around shear zones or plate boundary regions.

586

587 **Acknowledgements**

588 This work was supported by the University of Lausanne.

589 All numerical results have been generated with a self-developed MATLAB algorithm, which
590 is available on the platform GitHub under: https://github.com/schmaste/HMC_Brucite.

591 E.M. acknowledges the Johannes Gutenberg University of Mainz for financial support. O.P.
592 was supported by an ERC starting grant “nanoEARTH” (852069). Y.P. was supported by the
593 Russian Ministry of Science and Higher Education (project No. 075-15-2019-1890)

594

595 **References**

596 Austrheim, H. (1987), Eclogitization of lower crustal granulites by fluid migration through
597 shear zones, Earth and Planetary Science Letters, 81(2-3), 221-232.

598 Beinlich, A., T. John, J. Vrijmoed, M. Tominaga, T. Magna, and Y. Podladchikov (2020),
599 Instantaneous rock transformations in the deep crust driven by reactive fluid flow, Nature
600 Geoscience, 13(4), 307-311.

601 Biot, M. A. (1941), General theory of three-dimensional consolidation, J. Appl. Phys.,
602 12(February), 155-164.

603 Brantut, N., J. Sulem, and A. Schubnel (2011), Effect of dehydration reactions on earthquake
604 nucleation: Stable sliding, slow transients, and unstable slip, Journal of Geophysical
605 Research: Solid Earth, 116(B5).

606 Carmichael, D. M. (1987), Induced stress and secondary mass transfer: thermodynamic basis
607 for the tendency toward constant-volume constraint in diffusion metasomatism, in
608 Chemical transport in metasomatic processes, edited, pp. 239-264, Springer.

609 Chorin, A. J. (1968), Numerical solution of the Navier-Stokes equations, Mathematics of
610 computation, 22(104), 745-762.

611 Connolly, J. (1997), Devolatilization-generated fluid pressure and deformation-propagated
612 fluid flow during prograde regional metamorphism, Journal of Geophysical Research:
613 Solid Earth, 102(B8), 18149-18173.

614 Connolly, J. A. (2005), Computation of phase equilibria by linear programming: a tool for
615 geodynamic modeling and its application to subduction zone decarbonation, Earth and
616 Planetary Science Letters, 236(1-2), 524-541.

617 Dahlen, F. A. (1992), Metamorphism of nonhydrostatically stressed rocks, American Journal
618 of Science, 292(3), 184-198.

619 Duretz, T., L. Räss, Y. Podladchikov, and S. Schmalholz (2019), Resolving
620 thermomechanical coupling in two and three dimensions: spontaneous strain localization
621 owing to shear heating, Geophysical Journal International, 216(1), 365-379.

622 Escartin, J., G. Hirth, and B. Evans (1997), Effects of serpentinization on the lithospheric
623 strength and the style of normal faulting at slow-spreading ridges, Earth and Planetary
624 Science Letters, 151(3-4), 181-189.

625 Evans, O., M. Spiegelman, and P. B. Kelemen (2020), Phase-Field Modeling of Reaction-
626 Driven Cracking: Determining Conditions for Extensive Olivine Serpentinization, Journal
627 of Geophysical Research: Solid Earth, 125(1), e2019JB018614.

628 Ferrand, T. P., N. Hilairet, S. Incel, D. Deldicque, L. Labrousse, J. Gasc, J. Renner, Y. Wang,
629 H. W. Green Ii, and A. Schubnel (2017), Dehydration-driven stress transfer triggers
630 intermediate-depth earthquakes, Nature communications, 8(1), 1-11.

631 Gerya, T. (2019), Introduction to numerical geodynamic modelling, Cambridge University
632 Press.

633 Gerya, T. V., J. A. Connolly, and D. A. Yuen (2008), Why is terrestrial subduction one-
634 sided?, Geology, 36(1), 43-46.

635 Gomberg, J., Cascadia, and B. W. Group (2010), Slow-slip phenomena in Cascadia from
636 2007 and beyond: A review, Bulletin, 122(7-8), 963-978.

637 Guillot, S., S. Schwartz, B. Reynard, P. Agard, and C. Prigent (2015), Tectonic significance
638 of serpentinites, Tectonophysics, 646, 1-19.

639 Holland, T., and R. Powell (1998), An internally consistent thermodynamic data set for
640 phases of petrological interest, Journal of metamorphic Geology, 16(3), 309-343.

641 Jamtveit, B., H. Austrheim, and A. Malthe-Sørenssen (2000), Accelerated hydration of the
642 Earth's deep crust induced by stress perturbations, Nature, 408(6808), 75-78.

643 Jamtveit, B., E. Moulas, T. B. Andersen, H. Austrheim, F. Corfu, A. Petley-Ragan, and S. M.
644 Schmalholz (2018), High Pressure Metamorphism Caused by Fluid Induced Weakening of
645 Deep Continental Crust, Scientific Reports, 8(1), 17011, doi:10.1038/s41598-018-35200-1.

646 Jamtveit, B., A. Petley-Ragan, S. Incel, K. G. Dunkel, C. Aupart, H. Austrheim, F. Corfu, L.
647 Menegon, and F. Renard (2019), The effects of earthquakes and fluids on the
648 metamorphism of the lower continental crust, Journal of Geophysical Research: Solid
649 Earth, 124(8), 7725-7755.

650 Jaquet, Y., and S. M. Schmalholz (2018), Spontaneous ductile crustal shear zone formation by
651 thermal softening and related stress, temperature and strain rate evolution, Tectonophysics,
652 746, 384-397.

653 John, T., M. Scambelluri, M. Frische, J. D. Barnes, and W. Bach (2011), Dehydration of
654 subducting serpentinite: implications for halogen mobility in subduction zones and the
655 deep halogen cycle, Earth and Planetary Science Letters, 308(1-2), 65-76.

656 Jolivet, L., H. Raimbourg, L. Labrousse, D. Avigad, Y. Leroy, H. Austrheim, and T. B.
657 Andersen (2005), Softening trigerred by eclogitization, the first step toward exhumation
658 during continental subduction, Earth and Planetary Science Letters, 237(3-4), 532-547,
659 doi:10.1016/j.epsl.2005.06.047.

660 Kelemen, P. B., and G. Hirth (2012), Reaction-driven cracking during retrograde
661 metamorphism: Olivine hydration and carbonation, Earth and Planetary Science Letters,
662 345, 81-89.

663 Kelemen, P. B., and J. Matter (2008), In situ carbonation of peridotite for CO2 storage,
664 Proceedings of the National Academy of Sciences, 105(45), 17295-17300.

665 Kuleci, H., O. Ulven, E. Rybacki, B. Wunder, and R. Abart (2017), Reaction-induced
666 fracturing in a hot pressed calcite-periclase aggregate, Journal of Structural Geology, 94,
667 116-135.

668 Lasaga, A. C. (1986), Metamorphic reaction rate laws and development of isograds,
669 Mineralogical Magazine, 50(357), 359-373.

670 Llana-Fúnez, S., J. Wheeler, and D. R. Faulkner (2012), Metamorphic reaction rate controlled
671 by fluid pressure not confining pressure: implications of dehydration experiments with
672 gypsum, Contributions to Mineralogy and Petrology, 164(1), 69-79.

673 Malvoisin, B., H. Austrheim, G. Hetényi, J. Reynes, J. Hermann, L. P. Baumgartner, and Y.
674 Y. Podladchikov (2020), Sustainable densification of the deep crust, Geology, 48(7), 673-
675 677, doi:10.1130/g47201.1.

676 Malvoisin, B., Y. Y. Podladchikov, and J. C. Vrijmoed (2015), Coupling changes in densities
677 and porosity to fluid pressure variations in reactive porous fluid flow: local thermodynamic
678 equilibrium, Geochemistry, Geophysics, Geosystems, 16(12), 4362-4387.

679 Moulas, E., J.-P. Burg, and Y. Podladchikov (2014), Stress field associated with elliptical
680 inclusions in a deforming matrix: Mathematical model and implications for tectonic
681 overpressure in the lithosphere, Tectonophysics, 631, 37-49,
682 doi:10.1016/j.tecto.2014.05.004.

683 Moulas, E., S. M. Schmalholz, Y. Podladchikov, L. Tajčmanová, D. Kostopoulos, and L.
684 Baumgartner (2019), Relation between mean stress, thermodynamic, and lithostatic
685 pressure, Journal of metamorphic geology, 37(1), 1-14.

686 Omlin, S., B. Malvoisin, and Y. Y. Podladchikov (2017), Pore fluid extraction by reactive
687 solitary waves in 3-D, Geophysical Research Letters, 44(18), 9267-9275.

688 Philpotts, A. R., and J. J. Ague (2009), Principles of Ingeous and Metamorphic Petrology,
689 Second ed., 667 pp., Cambridge University Press, Cambridge.

690 Plümper, O., T. John, Y. Y. Podladchikov, J. C. Vrijmoed, and M. Scambelluri (2017), Fluid
691 escape from subduction zones controlled by channel-forming reactive porosity, Nature
692 Geoscience, 10(2), 150-156.

693 Plümper, O., A. Røyne, A. Magrasó, and B. Jamtveit (2012), The interface-scale mechanism
694 of reaction-induced fracturing during serpentinization, Geology, 40(12), 1103-1106.

695 Putnis, A. (2009), Mineral replacement reactions, Reviews in mineralogy and geochemistry,
696 70(1), 87-124.

697 Quinquis, M., and S. Buiter (2014), Testing the effects of basic numerical implementations of
698 water migration on models of subduction dynamics, Solid Earth, 5(1), 537.

699 Räss, L., T. Duretz, and Y. Podladchikov (2019), Resolving hydromechanical coupling in two
700 and three dimensions: spontaneous channelling of porous fluids owing to decompaction
701 weakening, Geophysical Journal International, 218(3), 1591-1616.

702 Schmalholz, S. M., and N. S. Mancktelow (2016), Folding and necking across the scales: a
703 review of theoretical and experimental results and their applications, Solid Earth, 7(5),
704 1417-1465, doi:10.5194/se-7-1417-2016.

Schmalholz, S. M., S. Medvedev, S. M. Lechmann, and Y. Podladchikov (2014), Relationship between tectonic overpressure, deviatoric stress, driving force, isostasy and gravitational potential energy, Geophysical Journal International, 197(2), 680-696, doi:10.1093/gji/ggu040.

Schmalholz, S. M., and Y. Podladchikov (2014), Metamorphism under stress: The problem of relating minerals to depth, Geology, 42(8), 733-734, doi:10.1130/focus0822014.1.

Schmalholz, S. M., and Y. Y. Podladchikov (2013), Tectonic overpressure in weak crustal-scale shear zones and implications for the exhumation of high-pressure rocks, Geophysical Research Letters, 40(10), 1984-1988, doi:10.1002/grl.50417.

Schmalholz, S. M., and D. W. Schmid (2012), Folding in power-law viscous multi-layers, Philosophical Transactions of the Royal Society a-Mathematical Physical and Engineering Sciences, 370(1965), 1798-1826, doi:10.1098/rsta.2011.0421.

Schmid, D. W., and Y. Y. Podladchikov (2003), Analytical solutions for deformable elliptical inclusions in general shear, Geophysical Journal International, 155, 269-288.

Wheeler, J. (2018), The effects of stress on reactions in the Earth: sometimes rather mean, usually normal, always important, Journal of Metamorphic Geology, 36(4), 439-461.

Yang, J., and M. Faccenda (2020), Intraplate volcanism originating from upwelling hydrous mantle transition zone, Nature, 579(7797), 88-91.

Yarushina, V. M., and Y. Y. Podladchikov (2015), (De) compaction of porous viscoelastoplastic media: Model formulation, Journal of Geophysical Research: Solid Earth, 120(6), 4146-4170.

726 Zheng, X., B. Cordonnier, W. Zhu, F. Renard, and B. Jamtveit (2018), Effects of confinement
727 on reaction-induced fracturing during hydration of periclase, Geochemistry, Geophysics,
728 Geosystems, 19(8), 2661-2672.

729

730

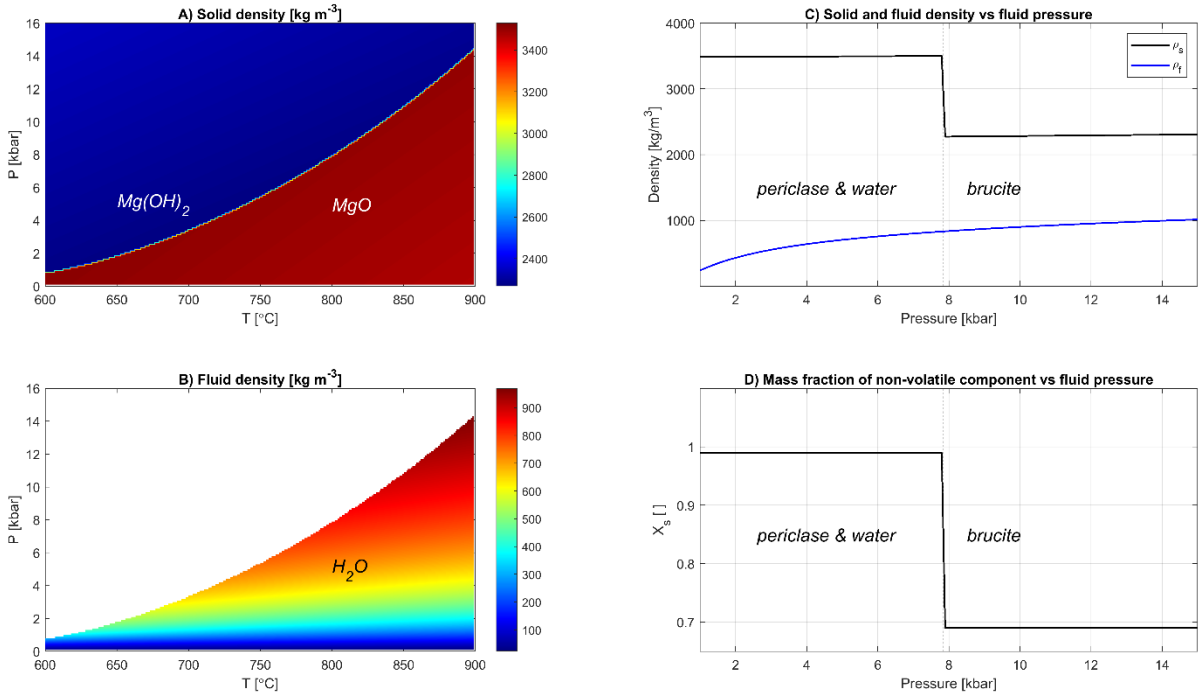

731

732 Figure 1. Solid (A) and fluid (B) density fields in pressure, P, and temperature, T, space.

733 Corresponding profiles of solid and fluid densities and mass fraction of MgO as a function of

734 fluid pressure at 800 °C (C and D). These three profiles are used in the numerical algorithm as

735 pre-calculated data.

736

737

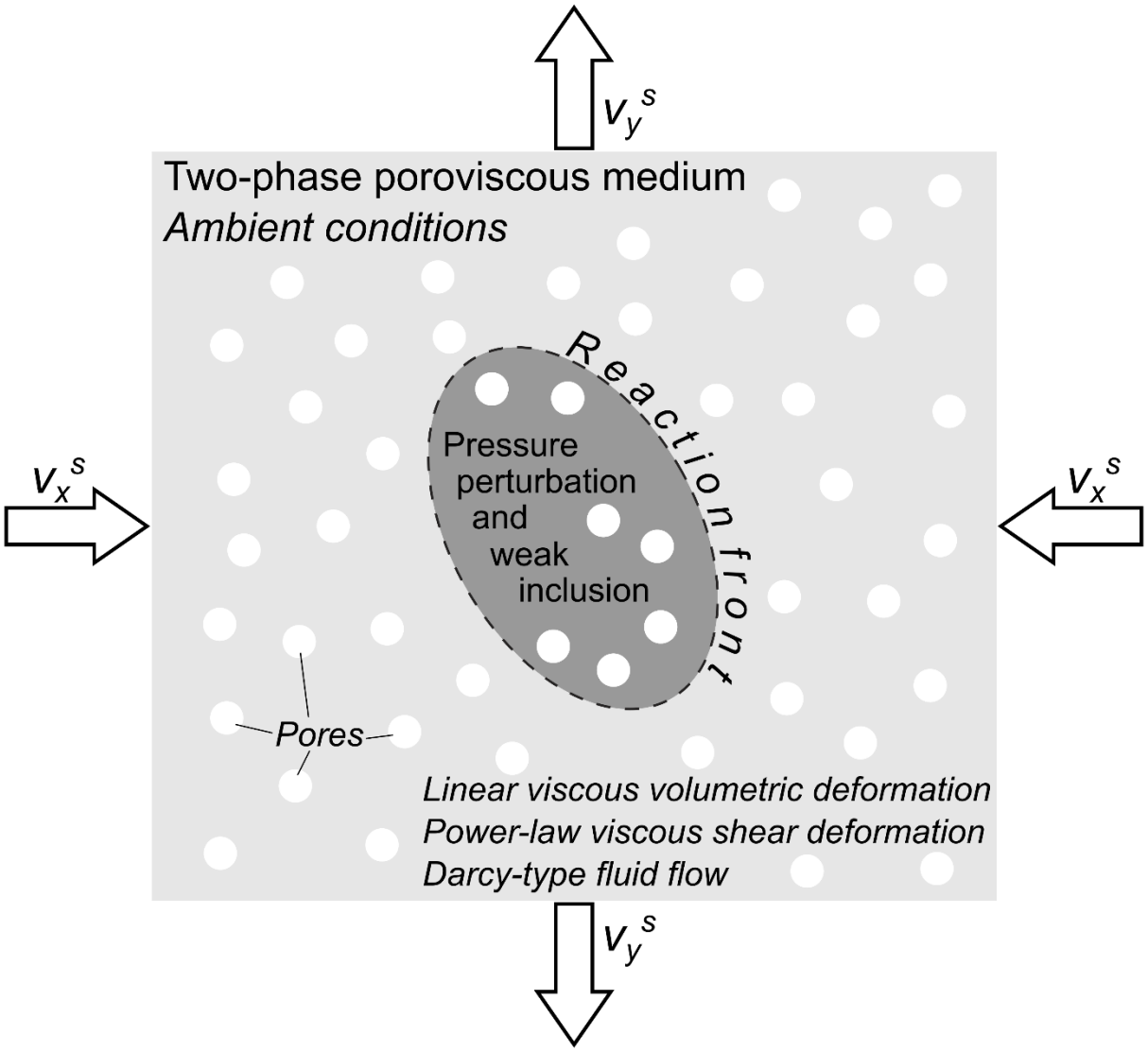

738

739 Figure 2. Sketch of the modelled scenario and the model configuration (see text for details).

740

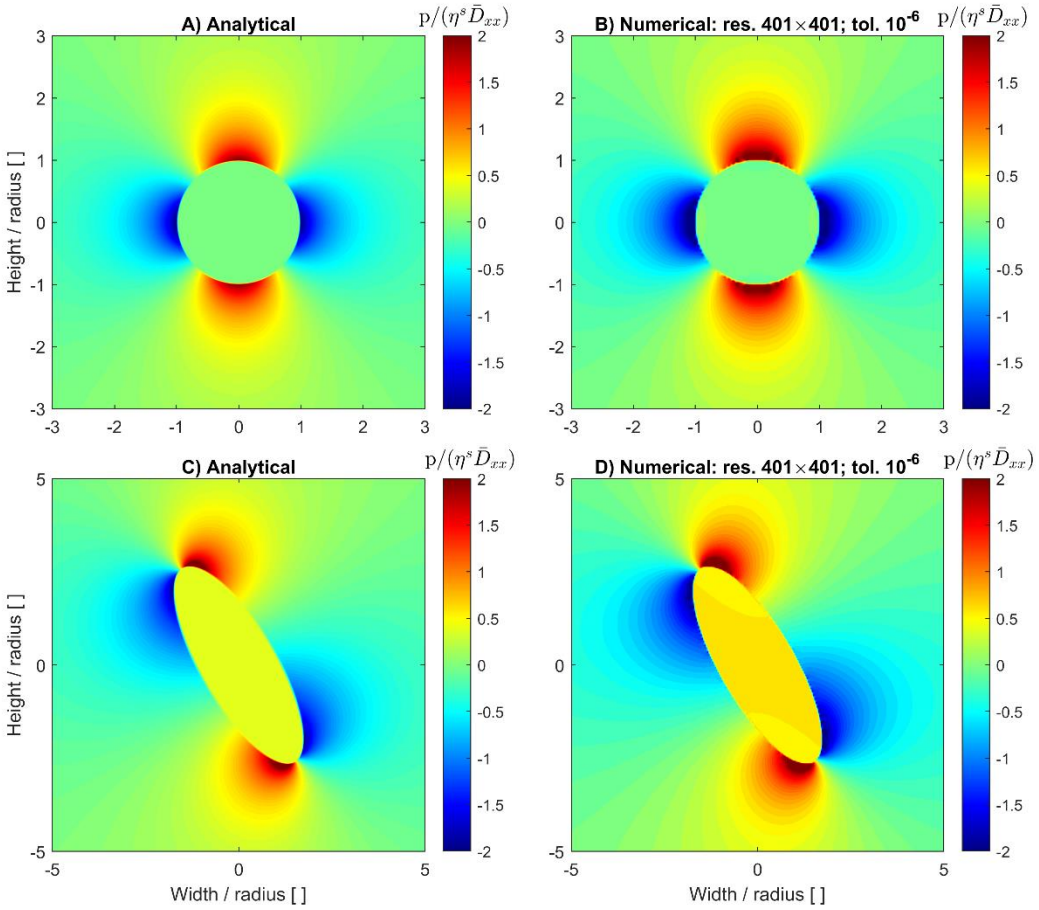

Figure 3. Numerical results of the mechanical model without fluid flow and reaction. A) and C) Total pressure field from analytical solutions of Moulas et al., 2014 for a weak circular and weak oblique elliptical inclusion under horizontal shortening. B) and D) corresponding numerical results. The numerical model reproduces the characteristic pressure distribution and magnitudes.

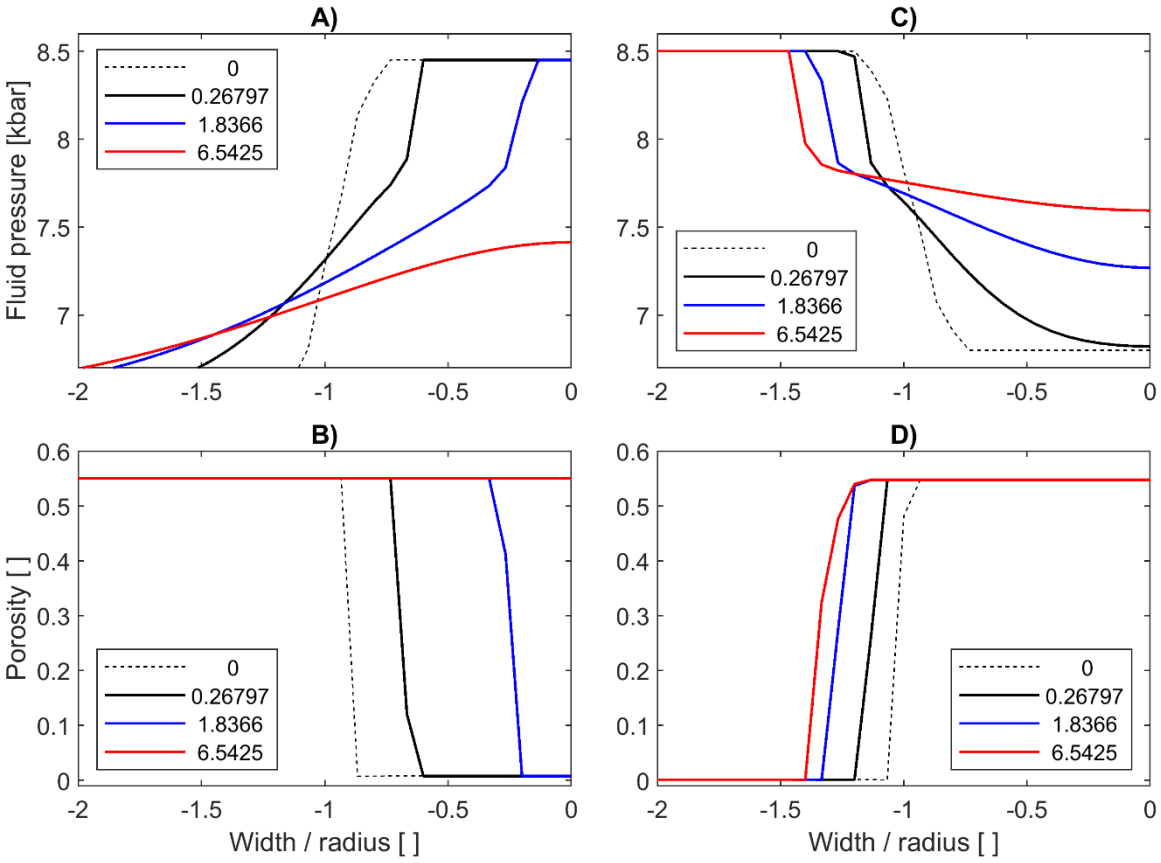

Figure 4. Numerical results of the hydro-chemical model, for which solid velocities are set to zero. Evolution of fluid pressure for positive (A) and negative (C) initial pressure perturbations in circular inclusion. Corresponding evolution of porosity (B and D). Numbers in legend indicate modelled time in hours.

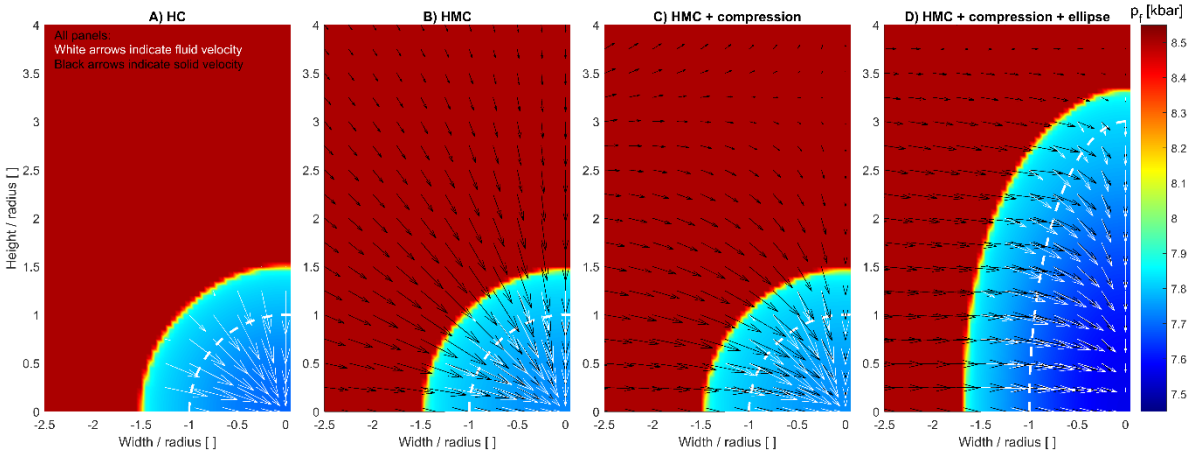

Figure 5. Colorplot indicating the distribution of fluid pressure, p_f , and arrows indicating fluid (white arrows) and solid (black arrows) velocities for four simulations at a model time of 39.2 hours. The circular and elliptical inclusion exhibited initially a smaller fluid pressure than the surrounding and the shear viscosity is a factor 1000 smaller than the one of the surrounding (see text for details). A) Hydro-Chemical (HC) model (solid velocities are zero) with circular inclusion and no far-field shortening. B) Hydro-Mechanical-Chemical (HMC) with circular inclusion and no far-field shortening. C) HMC with circular inclusion and with far-field shortening. D) HMC with elliptical inclusion of initial aspect ratio of three and with far-field shortening. The white dashed line indicates the initial size of the perturbation.

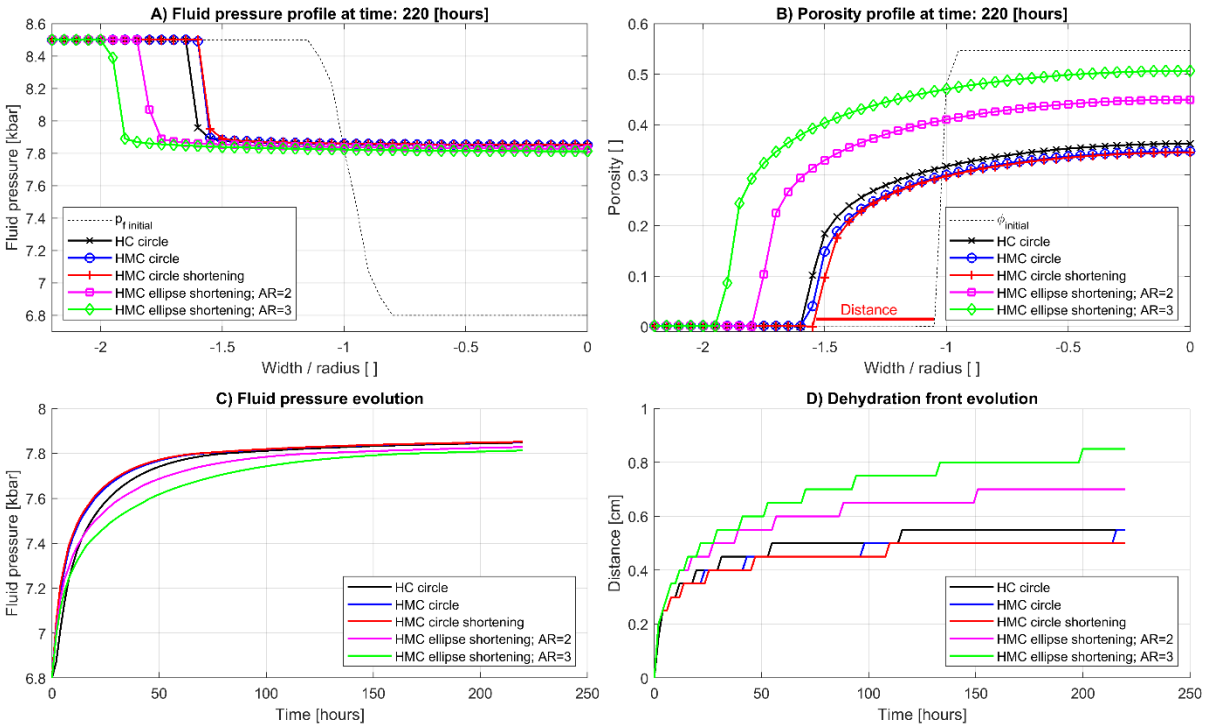

Figure 6. Horizontal profiles of fluid pressure and porosity for the models presented in figure 5 and an additional model with elliptical inclusion having an initial aspect ratio of two. The profiles are at the vertical middle of the model domain corresponding to the bottom of the color plots displayed in figure 5. Profile of fluid pressure (A) and porosity (B) for a modelled time of 220 hours. C) Time evolution of fluid pressure in the center of the inclusion corresponding to horizontal location 0 in A). D) Time evolution of the distance between the current location of the dehydration front and the initial location. This distance is indicated by the width of the horizontal red line in B) for the HMC model with circular inclusion and shortening (red line).

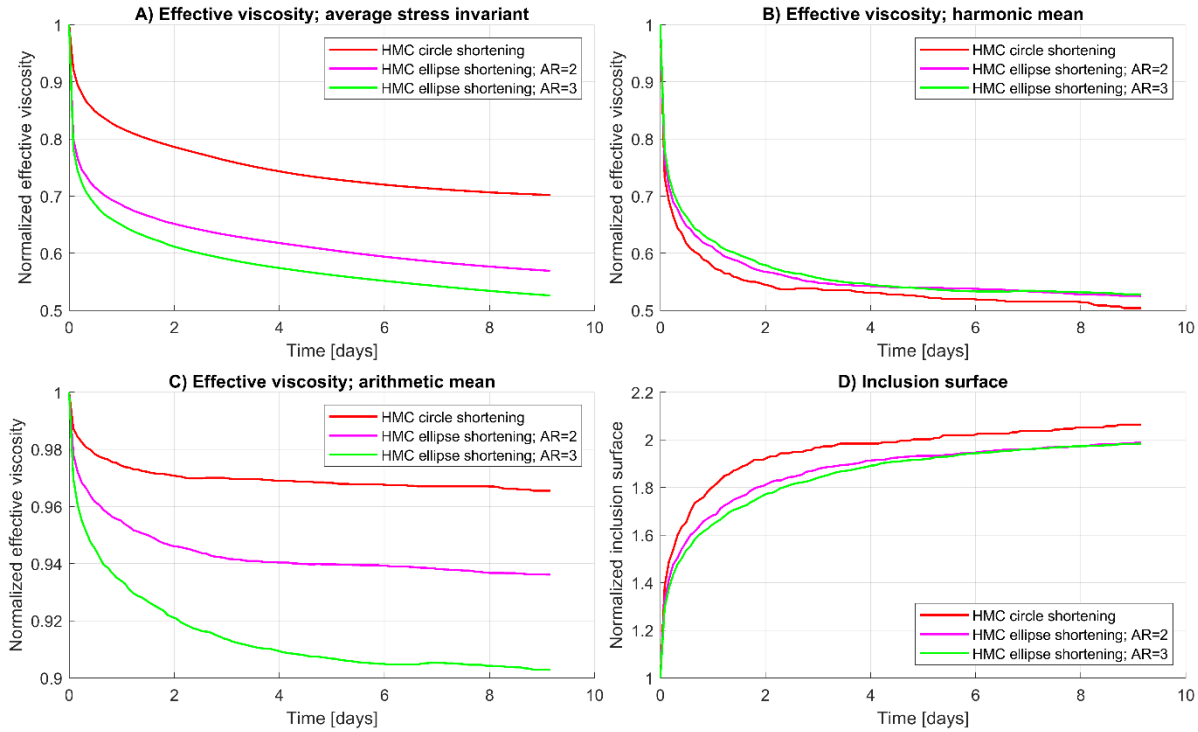

Figure 7. Reaction-induced weakening with progressive time is quantified by the decrease of the effective viscosity (A to C) of the entire model domain of three simulations presented in figure 6 (see legends). A) The effective viscosity is calculated by the area-average of the second invariant of the stress tensor divided by the second invariant of the far-field, pure-shear, strain rate invariant, which is constant throughout the simulation. B) The effective viscosity is calculated by the harmonic mean of all viscosities at all numerical grid points. C) Same as B) but for arithmetic average. All effective viscosities are divided, normalized, by the initial effective viscositiy of the first numerical time step. D) Relative increase of the inclusion surface, divided by initial inclusion surface, with time.

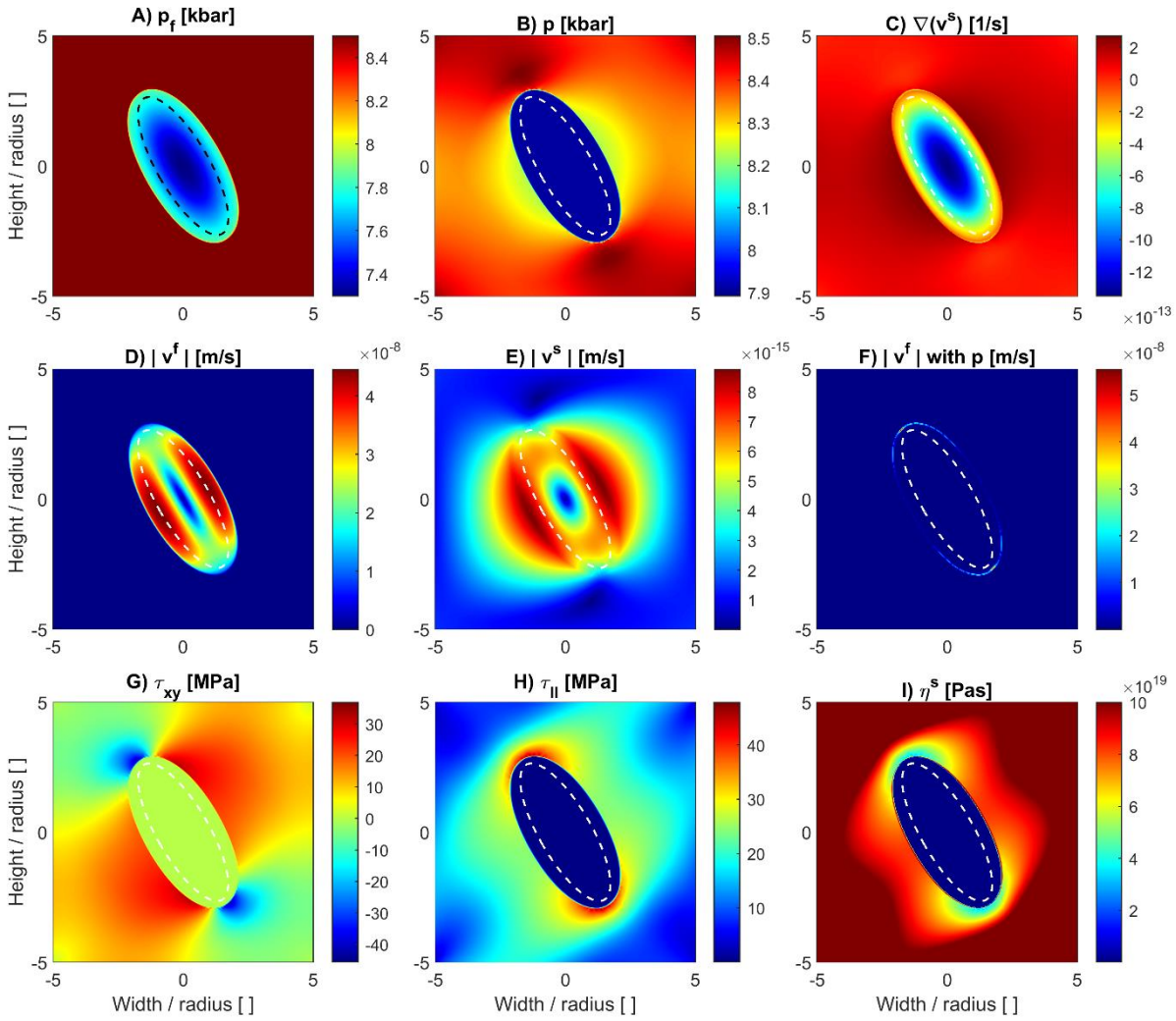

Figure 8. Colormaps of model quantities (see table 1) for an oblique elliptical inclusion with far-field horizontal pure shear shortening after a modelled time corresponding to 16.5 hours. The material is power-law viscous with a stress exponent of 3, and the inclusion has a shear viscosity thousand times smaller than the surrounding.

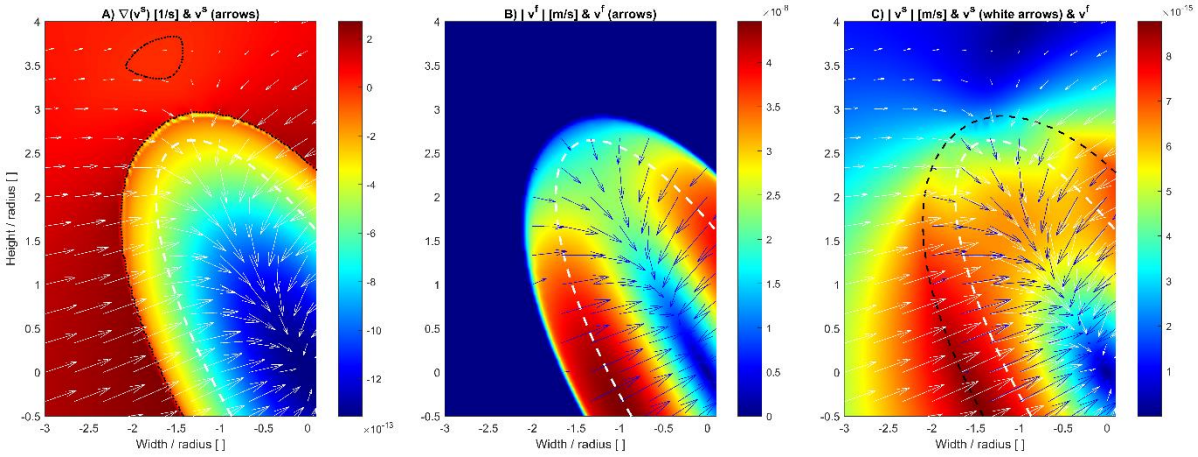

Figure 9. Enlargement of model results displayed in figure 7. A) Colorplot of divergence of solid velocity field and arrows indicating solid velocity field. The dashed white line indicates the initial inclusion boundary and a black dotted line indicates the contour for which the divergence is zero. B) Colorplot of the absolute magnitude of fluid velocity and arrows indicating fluid velocity field. C) Colorplot of the absolute magnitude of solid velocity and arrows indicating solid velocity field. Black dashed line indicates current reaction front.

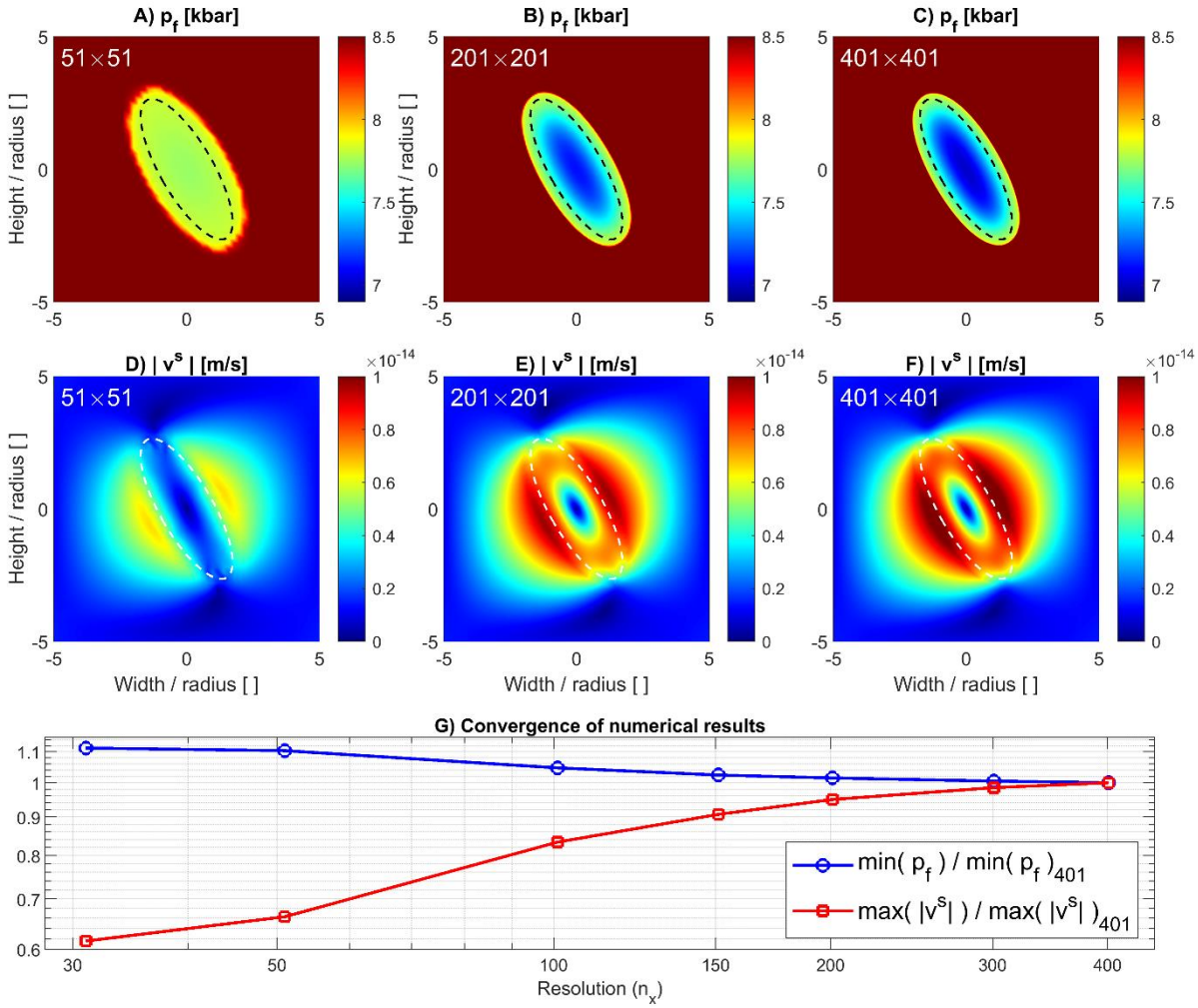

812

813 Figure 10. Numerical convergence test for the model of figure 7 at a model time

814 corresponding to 3.3 hours. A) to C) shows color plot of p_f for three different numerical

815 resolutions (white numbers inside panel). D) to F) shows color plot of $|\mathbf{v}^s|$ for three different

816 numerical resolutions (white numbers inside panel). G) Variation of the minimum value of

817 p_f and the maximal value of $|\mathbf{v}^s|$ with increasing resolution. The horizontal axis shows the

818 resolution in the horizontal x-direction, and the vertical axis shows the corresponding

819 quantities for p_f and $|\mathbf{v}^s|$ divided by the corresponding value for the maximal resolution of

820 401 grid points. The plot shows that the respective values vary less and less with increasing

821 resolution indicating a convergence of the numerical result towards a specific magnitude.

822

823 Table 1. Model variables and parameters.

Symbol	Name	Units
p_f	Fluid pressure	$[Pa]$
φ	Porosity	[ ]
ρ_s	Solid density	$\left[kg \cdot m^{-3}\right]$
ρ_f	Fluid density	$\left[kg \cdot m^{-3}\right]$
X_s	Mass fraction MgO	[ ]
p	Total pressure	$[Pa]$
$v_x^s,\ v_y^s$	Solid velocities	$\left[m \cdot s^{-1}\right]$
$v_x^f,\ v_y^f$	Fluid velocities	$\left[m \cdot s^{-1}\right]$
$\tau_{xx}, \tau_{yy}, \tau_{xy}$	Deviatoric stresses	$[Pa]$
τ_{ref}	Reference stress	$[Pa]$
k	Permeability	$\left[m^2\right]$
η_f	Fluid viscosity	$[Pa \cdot s]$
η^s	Shear viscosity solid	$[Pa \cdot s]$
λ	Bulk viscosity solid	$[Pa \cdot s]$
n	Stress exponent	[ ]
β_{eff}	Eff. compressibility	$[Pa]$
p_{ini}	Initial ambient pressure	$[Pa]$
$\bar{D}_{xx}$	Far-field shortening rate	$\left[s^{-1}\right]$
r	Inclusion radius	$[m]$
w	Model width	$[m]$

824